Li–O_2 Batteries Very Important Paper

How to cite: Angew. Chem. Int. Ed. 2022, 61, e202116635
International Edition: doi.org/10.1002/anie.202116635
German Edition: doi.org/10.1002/ange.202116635

Soluble and Perfluorinated Polyelectrolyte for Safe and High-Performance Li–O_2 Batteries

*Qi Xiong[+], Gang Huang[+], Yue Yu, Chao-Le Li, Jian-Chen Li, Jun-Min Yan, and Xin-Bo Zhang**

Abstract: The severe performance degradation of high-capacity Li–O_2 batteries induced by Li dendrite growth and concentration polarization from the low Li^+ transfer number of conventional electrolytes hinder their practical applications. Herein, lithiated Nafion (LN) with the sulfonic group immobilized on the perfluorinated backbone has been designed as a soluble lithium salt for preparing a less flammable polyelectrolyte solution, which not only simultaneously achieves a high Li^+ transfer number (0.84) and conductivity (2.5 mS cm^{-1}), but also the perfluorinated anion of LN produces a LiF-rich SEI for protecting the Li anode from dendrite growth. Thus, the Li–O_2 battery with a LN-based electrolyte achieves an all-round performance improvement, like low charge overpotential (0.18 V), large discharge capacity (9508 mAh g^{-1}), and excellent cycling performance (225 cycles). Besides, the fabricated pouch-type Li–air cells exhibit promising applications to power electronic equipment with satisfactory safety.

Introduction

As commercial Li-ion batteries approach their achievable energy densities, it is becoming more difficult to satisfy the growing demand of higher capacity for long-lasting electric devices. Developing an advanced rechargeable battery has the possibility to solve this dilemma. Among the various battery systems, nonaqueous Li–O_2 batteries with an ultra-high specific energy density of 3460 Wh kg^{-1}, more than two times higher than that of current Li-ion batteries, stand out.[1] Despite being promising, the conventional electrolytes with a typical Li^+ transfer number of around 0.2–0.5 can induce concentration gradients,[2] then the superfluous anions accumulated on the electrode will cause a severe potential drop for a large concentration polarization, leading to a loss of energy density and rate capability of the battery. Encouragingly, electrolytes with a high Li^+ transfer number can alleviate this phenomenon even though the conductivities are much lower than conventional electrolytes.[3] This has made single Li^+ conductors, like ceramic electrolytes, a research hotspot in recent years. However, given the fragile nature and large interface and grain boundary resistances of the ceramic electrolytes, their commercialization has a long way to go.[3a,4] Solid polymer electrolytes with inorganic fillers (such as ZrO_2, TiO_2, SiO_2, Al_2O_3, etc.) and solid polyelectrolytes with the anions immobilized on a polymer backbone can restrict the movement of anions, resulting in a high Li^+ transfer number, but all of them present rather poor conductivity (< 0.01 mS cm^{-1}) compared to the conventional electrolytes (1–10 mS cm^{-1}) at room temperature, and thus cannot meet the requirements for enabling a high-performance battery.[2,3,5] Different from them, polyelectrolyte solutions, prepared by dissolving the polyelectrolytes in nonaqueous solvents, with a Li^+ transfer number of approaching unity and without significantly compromised conductivity, have recently been considered to be an extremely promising candidate for the next-generation nonaqueous electrolytes and can be compatible with the manufacturing techniques of current lithium-ion batteries.[3a,6] Unfortunately, the study of polyelectrolyte solutions is limited due to the fact that solid polyelectrolytes nearly cannot dissociate in the solvents typically used for batteries.[7] Although the highly polar DMSO possesses a high affinity to the charged group and the neutral polymer backbone of the polyelectrolyte, which makes it good at solubilizing the polyelectrolyte,[7] its instability towards the bare Li metal anode brings new challenges.[8] Consequently, there is no report about the utilization of polyelectrolyte solutions in rechargeable Li-metal batteries.

Besides the issues related to the electrolyte, the uncontrollable Li dendrite growth in the anode side of Li–O_2 batteries can induce performance degradation and lead to short-circuits, restricting the practical applications of the battery. During the past few decades, many strategies have been developed to prevent the Li dendrite growth, such as electrolyte regulation, artificial solid electrolyte interface (SEI) construction, etc. Among these strategies, building a robust SEI film by electrolyte regulation has been considered to be an efficient and convenient tool, which can also

[*] Q. Xiong,[+] C.-L. Li, Prof. J.-C. Li, Prof. J.-M. Yan
Key Laboratory of Automobile Materials, Ministry of Education, Department of Materials Science and Engineering, Jilin University
Changchun, 130022 (P. R. China)

Q. Xiong,[+] Prof. G. Huang,[+] Y. Yu, C.-L. Li, Prof. X.-B. Zhang
State Key Laboratory of Rare Earth Resource Utilization, Changchun Institute of Applied Chemistry, Chinese Academy of Sciences
Changchun, 130022 (P. R. China)
E-mail: xbzhang@ciac.ac.cn

Y. Yu, Prof. X.-B. Zhang
University of Science and Technology of China
Hefei, 230026 (P. R. China)

[+] These authors contributed equally to this work.

© 2022 Wiley-VCH GmbH

be compatible with the existing battery production lines.[9] The SEI film derived from the decomposition of electrolytes is usually composed of inorganic and organic components, and the inorganic components show a higher interface energy than that of organic components.[10] Among all of the inorganic components (LiF, Li_2CO_3, LiOH, Li_2O, etc.), LiF presents the highest interfacial energy of 73.28 meV Å^{-2}.[11] In addition, it also displays electronic insulation and the ability to uniformly alter the electric field gradient.[12] All these features make LiF a good candidate for building a useful SEI film to prevent the Li dendrite growth. Up to now, though many achievements have been made towards a LiF-rich SEI, realizing a stable SEI through electrolyte regulation is still full of challenges, not to mention the requirement to simultaneously satisfy the needs of high Li^+ transfer number and nonflammability for electrolytes.

Herein, a lithiated Nafion (LN) with sulfonic groups ($-SO_3^-$) immobilized on the perfluorinated polymer backbone has been proposed as a representative soluble polyelectrolyte in dimethyl sulfoxide (DMSO), which can simultaneously achieve a high Li^+ transfer number of 0.84 and a Li^+ conductivity comparable to that of liquid electrolytes (2.08 mS cm^{-1} at room temperature). Moreover, the anion (Nafion$^-$) of LN with a well-tuned lowest unoccupied molecular orbital (LUMO) energy level can be preferentially decomposed into a LiF-rich and stable SEI, ensuring the prevention of Li dendrite growth and the long-term cycling of the Li-metal anode. Besides, this new polyelectrolyte solution also exhibits flame retardancy. Therefore, the Li–O_2 batteries with LN in DMSO can promote the solution discharge process with a large discharge capacity (9508 mAh g^{-1} at 200 mA g^{-1}), and enable an excellent rate capability. Furthermore, the batteries show an ultralow charge overpotential (0.18 V) with a high round-trip energy efficiency (88.5 %) in the 1st cycle and outstanding cycle performance (225 cycles at a limited capacity of 1000 mAh g^{-1}). The fabricated pouch-type Li–air cells with this less flammable polyelectrolyte solution incisively and vividly present high safety. The nail penetration and corner-cutting tests do not disturb the cells to power red light-emitting diodes (LEDs), electric fans, smartwatches, and smartphones, promoting the Li–O_2 batteries to be used for next-generation energy storage.

Results and Discussion

Polyelectrolyte Design

To prepare a polyelectrolyte solution with a high Li^+ transfer number and an ability to construct a robust LiF-rich SEI, a desirable polyelectrolyte should be first designed. The incorporation of F atoms into the molecular skeleton can lower its LUMO energy level,[13] making the molecule susceptible to decomposition prior to the solvent to produce a LiF-rich SEI for protecting the Li anode from dendrite growth and DMSO induced corrosion. With this in mind, lithiated Nafion (LN), a kind of perfluorosulfonic ionomer with the $-SO_3^-$ anions fixed on the side chains of a perfluorinated polymer backbone, could meet all the requirements and thus has been chosen as a representative soluble polyanionic Li salt to behave as the polyelectrolyte (Scheme 1).

As a proof-of-concept, the molecular orbital energy levels of the molecules were firstly investigated by density functional theory (DFT) calculations to check whether the anion of the LN could be decomposed earlier than the solvent to engender a stable SEI layer.[14] DMSO was selected as the solvent for its high stability[8,15] and the ability to dissolve LN. Additionally, the molecular orbital energy levels of other commonly used lithium salts in Li–O_2 batteries were also calculated as a comparison. As shown in Figure 1a, Nafion$^-$ displays a lower LUMO energy level than DMSO and the other anions; the LUMO is mainly located on the perfluorinated backbone, ensuring its preferential reduction to produce the LiF-rich component in SEI. Besides, NO_3^- and bis(trifluoromethane)sulfonamide anions (TFSI$^-$) just exhibit slightly lower LUMO energy levels than DMSO, indicating their potential ability to produce anion-derived SEI with rich inorganic components. Then, these three Li salts and the popularly used salt of $LiCF_3SO_3$, which also contains the same anion ($-SO_3^-$) as Nafion$^-$, were selected to respectively prepare the electrolyte for further analysis. The physical properties of the electrolytes with a concentration of 0.5 M were studied first. Due to the restricted movement of the anion, LN-DMSO shows the highest Li^+ transfer number of 0.84 (Figure 1b; Supporting Information, Figure S1 and Table S1), meanwhile, it also offers a comparable Li^+ conductivity (2.08 mS cm^{-1}) with the other three electrolytes (Figure 1b; Supporting Information, Figure S2). It should be mentioned that this conductivity of LN-DMSO (2.5 mS cm^{-1}; Supporting Information, Figure S2) is the highest value among all the reported polyelectrolyte solutions (Supporting Information, Table S2). As Li^+ desolvation is a key rate-determining step for Li deposition,[16] temperature-dependent electrochemical impedance spectra (EIS) were carried out. Just as shown in the Supporting Information, Figure S3 and S4, LN-DMSO possesses the lowest desolvation energy barrier

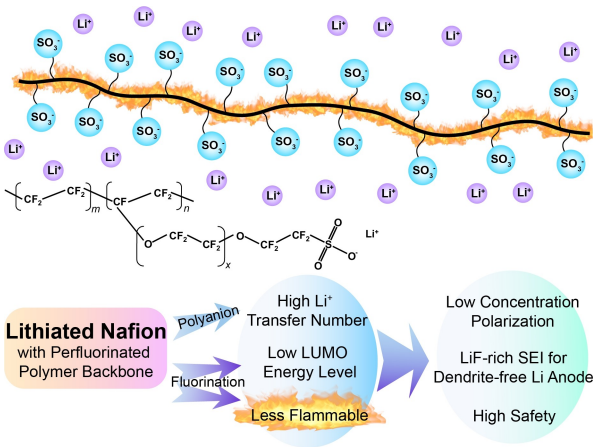

Scheme 1. Schematic illustration of the design principle of the polyelectrolyte.

© 2022 Wiley-VCH GmbH

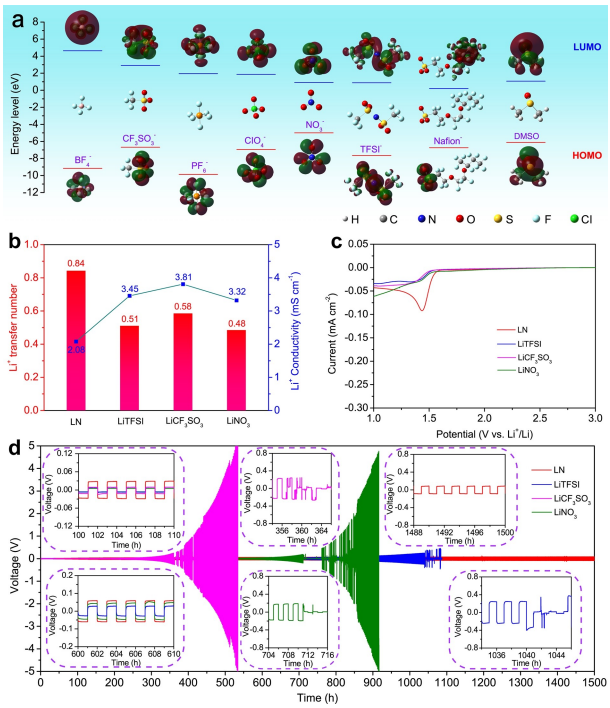

Figure 1. a) Molecular orbital energy levels of the salt anions and DMSO. b) Li^+ transfer number and Li^+ conductivity of the electrolytes. c) LSV of the electrolytes at 0.1 mV s^{-1}. d) Cycling performance of Li||Li symmetric cells under O_2 atmosphere and at a current density of 0.1 mA cm^{-2}.

(32.4 kJ mol^{-1}) among the four electrolytes, revealing its superiority for improving the mass transfer and electrode kinetics.

The reduction behavior of the salt anions were then studied by checking the electrochemical windows of the electrolytes through linear sweep voltammetry (LSV) to verify whether they follow the results of DFT calculations. As expected, LN-DMSO shows a sharp reduction peak with the highest onset reduction potential (Figure 1c) due to the perfluorinated backbone of Nafion$^-$, in accordance with the results of the DFT calculations. However, NO_3^-, TFSI$^-$ and $CF_3SO_3^-$ with a slightly lower or higher LUMO energy level than the solvent (DMSO) display similar onset reduction potentials, indicating the accompanied solvent decomposition. Since the SEI derived from the decomposition of the solvent is mainly composed of organic components, which has a lower interfacial energy than the inorganic components, making it insufficient to suppress the Li dendrite growth. The SEI derived from the preferential decomposition of anions is mainly composed of inorganic components, especially for the perfluorosulfonic polyanions here, which can offer LiF-rich decomposition products to better protect the Li metal. Besides, the electrolyte with LN also shows the highest oxidative stability (Supporting Information, Figure S5). To demonstrate the advantage of the LN-DMSO, the Li plating and stripping experiments of Li||Li symmetric batteries with the four electrolytes in an O_2 atmosphere were carried out. Unsurprisingly, the symmetric battery with LN presents an ultralong cycling lifetime of more than 1500 h under a current density of 0.1 mA cm^{-2} (Figure 1d). The symmetric batteries with LiTFSI, $LiNO_3$ and $LiCF_3SO_3$ can only operate for 1041, 711 and 357 h, respectively, before they short circuit. We hereafter select LiTFSI as a comparative lithium salt for LN due to the second longest lifetime of the Li metal in the batteries. Because the sole difference of the four electrolytes is the salt anion, we can deduce that the longest cycling performance of the Li metal in Li||Li symmetric batteries with LN could be attributed to the LiF-rich SEI, which is derived from the preferential decomposition of perfluorosulfonic polyanions before the solvent.

SEI Analysis and Li Deposition Behavior

To validate the above deduction, X-ray photoelectron spectroscopy (XPS) analysis was performed to identify the SEI components on the Li metal electrodes of the Li||Li symmetric batteries after 50 cycles. Based on the different forms of Li-containing compounds from the Li 1s spectrum in the SEI, it shows a dominant content of LiF (85.3 atom%) in the LN (Figure 2a; Supporting Information, Table S3), while this value is only 45.9 atom% in the LiTFSI (Figure 2c; Supporting Information, Table S3). Even performing Ar^+ sputtering for 5 minutes, the Li-containing compounds in the Li 1s XPS spectrum show that the content of LiF in the inner layer of SEI in the LN is still almost one time higher than that in the LiTFSI (26.4 atom% vs. 13.3 atom%, Figure 2a, c; Supporting Information, Table S3), manifesting the inorganic LiF-rich SEI layer enabled by the LN. F 1s spectra further confirm the presence of LiF in the SEI (Figure 2b, d), which originates from the reductive decomposition of the fluorine-containing lithium salts. To verify this, EIS spectra were employed to investigate the evolution of interfacial resistance (R_{int}) and charge transfer resistance (R_{ct}) in Li||Li symmetric batteries after different cycles. The battery with LN shows slowly increasing R_{int} and R_{ct} during the long-time plating/stripping process (Figure 2e; Supporting Information, Figure S6a). In contrast, the battery with LiTFSI displays decreased R_{int} and R_{ct} initially, which can be attributed to the Li dendrite growth induced surface area increase, then followed by a significant rise in R_{int} and R_{ct} (3 orders of magnitude larger than those of the battery with LN, Figure 2f; Supporting Information, Figure S6b, c). Subsequently, the morphology of the Li electrodes after 50 cycles was investigated by scanning electron microscopy (SEM). Evidently, the surface of the Li electrode in LN is relatively smooth with a SEI thickness of about 18 μm (Figure 2g, i). But the Li electrode in LiTFSI shows large cracks and pulverization with a SEI thickness of around 70 μm due to the Li dendrite growth induced continuous fracture and regeneration of the SEI and the persistently parasitic reaction of the exposed Li with the electrolyte (Figure 2h, j). Next, the deposition morphology of Li was investigated by SEM and in situ optical microscopy. It is clear that the deposited Li in LN exhibits dense and uniform morphology (Figure 2k) without observable dendrite growth (Figure 2m), whereas that in LiTFSI shows nodule-like

© 2022 Wiley-VCH GmbH

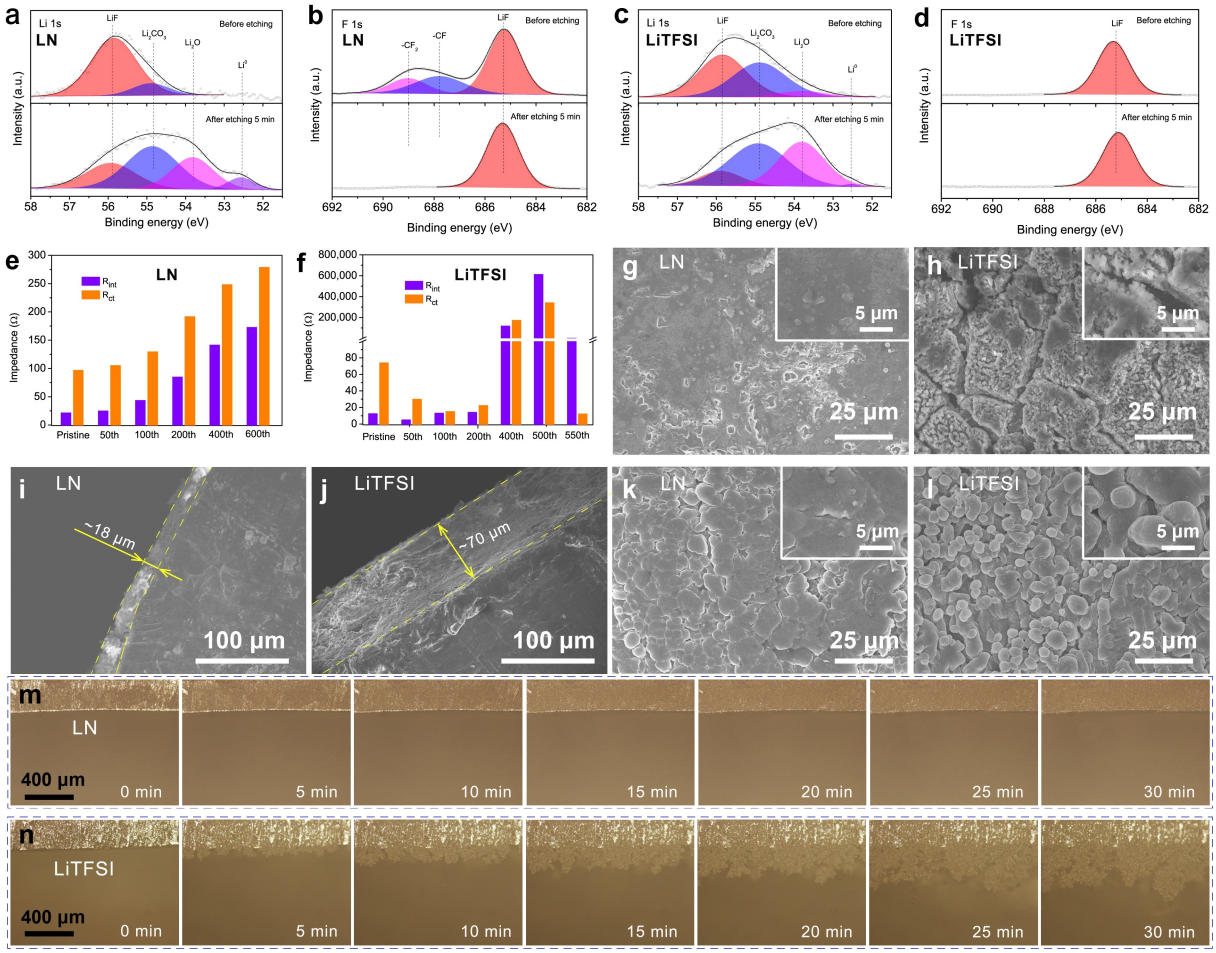

Figure 2. a)–d) XPS spectra of Li 1s (a, c) and F 1s (b, d) for the Li metals in LN (a, b) and LiTFSI (c, d) after 50 cycles. e), f) R_{int} and R_{SEI} of the Li||Li symmetric cells in LN (e) and LiTFS (f) after different cycles. g)–j) The morphology of the Li metals in Li||Li symmetric cells with LN (g) and LiTFSI (h) after 50 cycles, and the corresponding SEI thickness in LN (i) and LiTFSI (j). k), l) SEM images of the Li deposition morphology in LN (k) and LiTFSI (l) under an O_2 atmosphere and at a current density of 1 mA cm^{-2} with a plating capacity of 2 mAh cm^{-2}. m), n) In situ optical microscope images of the Li morphology evolution in LN (m) and LiTFSI (n) at a plating current density of 1 mA cm^{-2}.

morphology (Figure 2l) with severe dendrite growth (Figure 2n). The characterizations of the SEI ingredients, cycled Li morphology, and Li deposition behavior in $LiCF_3SO_3$ and $LiNO_3$ are also provided in the Supporting Information (Supporting Information, Figure S6–S12 and Table S3) to further demonstrate the advantages of the LN. Based on the above experimental evidence, we can draw a conclusion that the Nafion$^-$ with a well-tuned LUMO energy level can engender a LiF-rich SEI, enabling it to efficiently protect the Li anode and suppress Li dendrite growth.

Discharge Performance of Li–O_2 Batteries

After confirming the beneficial functions of the LN, its effects on the practically electrochemical performance of Li–O_2 batteries were firstly checked by galvanostatic discharge tests at different current densities. As shown in Figure 3a, the Li–O_2 battery with LN exhibits a good rate capability with a much larger discharge capacity of 9508 mAh g^{-1} at a current density of 200 mA g^{-1} than that with LiTFSI (6849 mAh g^{-1}), and even maintains a discharge capacity of 4240 mAh g^{-1} at a high current density of 2000 mA g^{-1}. After discharge, flake-typed products form on the cathode of the Li–O_2 battery with LiTFSI (Figure 3c), while enormously toroidal assemblies ($\approx$4 μm) accompanied by micrometer-sized particles emerge on that with LN (Figure 3b), which can be identified as Li_2O_2 by Fourier transform infrared (FTIR) spectra and X-ray diffraction (XRD) patterns (Figure 3d; Supporting Information, Figure S13). To shed light on the origin of the morphology difference for the discharge product, rotating ring-disk electrode (RRDE) measurements were carried out. Since the total oxygen reduction reaction (ORR) charge can be divided into two parts, one from the solution pathway and the other from the surface pathway, the proportion of the solution-mediated ORR charge can be calculated by dividing the ring charge (Q_{ring}) into the disk charge (Q_{disk}) and the collection efficiency (η) of RRDE,[17] and the η here is corrected to be 34.7 % (Supporting Information, Fig-

© 2022 Wiley-VCH GmbH

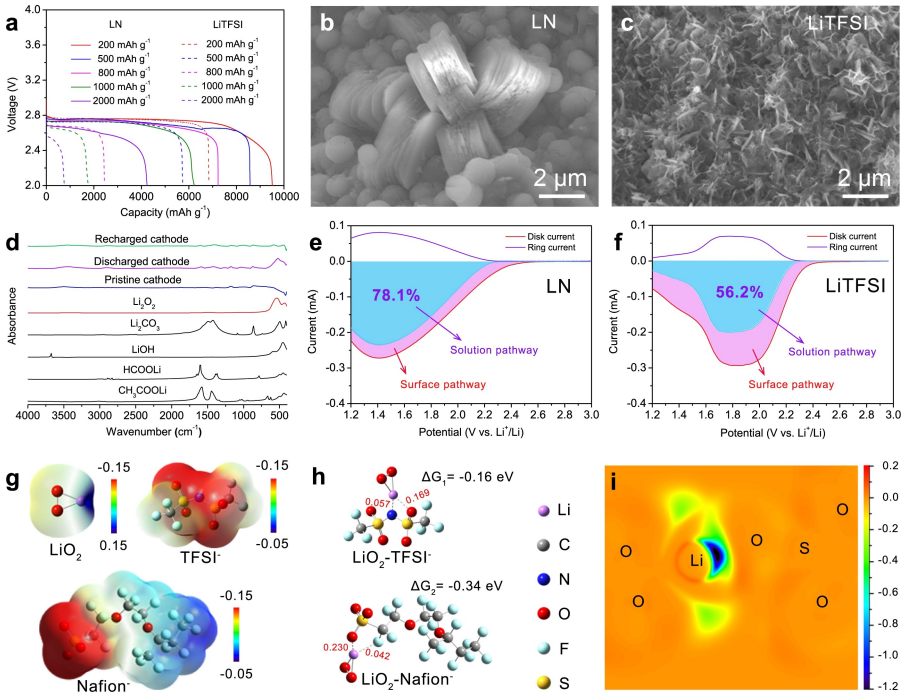

Figure 3. a) The discharge curves of the Li–O_2 batteries at different current densities. SEM images of the cathodes after discharge in b) LN and c) LiTFSI at a current density of 200 mA g^{-1}. d) FTIR spectra of the cathodes after discharge and recharge in LN. RRDE tests of the 0.1 M LN (e) and LiTFSI-based electrolytes (f). g) The surface electrostatic potential maps of the LiO_2, $TFSI^-$, and $Nafion^-$. h) The binding energies and the correspondingly optimized structures of the LiO_2 with $TFSI^-$ or $Nafion^-$. i) Color-filled difference map of ELF for the LiO_2-$Nafion^-$ with their monomers.

ure S14). Consequently, the proportion of the solution-mediated ORR charge with LN is quantitatively estimated to be 78.1 % (Figure 3e), much higher than that with LiTFSI (56.2 %; Figure 3f), indicating $Nafion^-$ can efficiently promote the solution discharge by increasing the solubility of the discharge intermediate (LiO_2) to generate large-sized Li_2O_2.

Subsequently, DFT calculations were employed to further unravel the salt anion induced changes of discharge mechanisms.[14,18] The surface electrostatic potential maps show that the negative charge of the $Nafion^-$ is dominantly located on $-SO_3^-$, while that of $TFSI^-$ is discretely distributed on the large sulfonimide group (Figure 3g), suggesting that there will be a stronger interaction between LiO_2 and $Nafion^-$, which is confirmed by the following thermodynamic and Mayer bond order analysis.[19] When anions bind with LiO_2, the overall Gibbs free energy change for $Nafion^-$ (−0.34 eV) is larger than that for $TFSI^-$ (−0.16 eV), and the total Mayer bond orders of Li–O (0.169) and Li–N (0.057) for $TFSI^-$ are lower than those of Li–O (0.230) and Li–F (0.042) for $Nafion^-$ (Figure 3h), clearly demonstrating the stronger interaction of LiO_2 with $Nafion^-$ than that with $TFSI^-$. After this, the difference maps of electron density and electron localization function (ELF) were employed to characterize the chemical bond between $-SO_3^-$ and LiO_2. As illustrated in Supporting Information, Figure S15, there is an obvious increase of electron density between the region of intermolecular interaction, indicating the electron transfer from $-SO_3^-$ to LiO_2, which is further supported by the decrease of electron localization near the Li atom induced by the Pauli repulsion effect (Figure 3i). The DFT calculations together with the experimental observations evidently prove that the $Nafion^-$ can promote solution discharge by strengthening its interaction with LiO_2.

Cycling Performance of Li–O_2 Batteries

Apart from discharge performance, the energy efficiency and cycling stability are also important indicators to evaluate the performance of Li–O_2 batteries. The 1st cycle discharge–charge curves of Li–O_2 batteries with LN and LiTFSI are shown in the Supporting Information, Figure S16. Though the battery with LN can facilitate the decomposition of Li_2O_2 in a relatively low charge voltage (Figure 3d; Supporting Information, Figure S17 and S18), its energy efficiency is still far away from the value that can enable the practical applications of Li–O_2 batteries, thus an excellent catalyst for reducing the charge overpotential is indispensable.

With the incorporation of the catalyst of RuO_2 nanoparticles coated on carbon nanotubes (RuO_2@CNTs),[1b,20] the Li–O_2 battery with LN exhibits an ultralow charge voltage of 3.13 V and a discharge–charge voltage gap of 0.30 V, obtaining an energy efficiency as high as 88.5 % (Figure 4a). Nevertheless, for the battery with LiTFSI, a higher charge voltage (3.21 V) and a larger discharge–charge voltage gap (0.38 V) are observed (Figure 4d). The lower

© 2022 Wiley-VCH GmbH

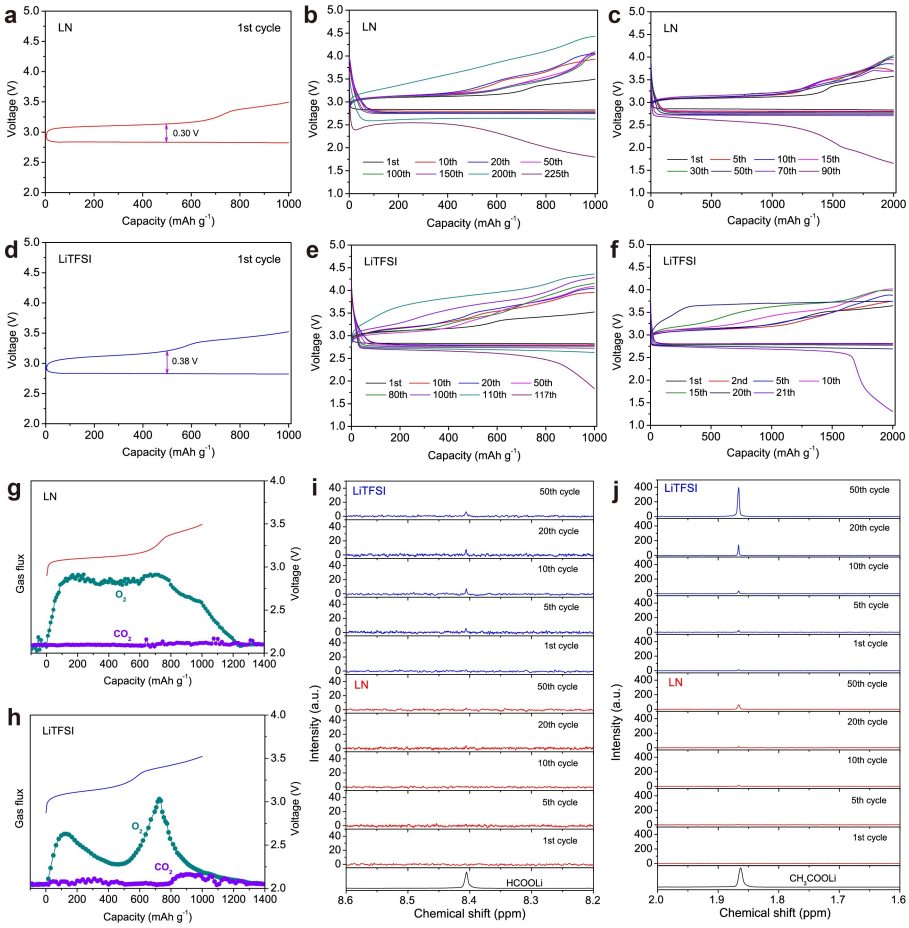

Figure 4. The first discharge–charge curves of the Li–O_2 batteries with a) LN and d) LiTFSI. b), c), e), f) Cycling performance of the Li–O_2 batteries with capacities of 1000 mAh g^{-1} (b, e) and 2000 mAh g^{-1} (c, f) at a current density of 500 mA g^{-1}. In situ gas evolution profiles of the Li–O_2 batteries with LN (g) and LiTFSI (h) during charge. ^{1}H NMR spectra of the cathodes of Li–O_2 batteries for HCOOLi (i) and CH_3COOLi (j) after different cycles.

overpotential of the battery with LN than that with LiTFSI can be attributed to the high Li^+ transfer number induced decrease of concentration polarization. Then, the cycling performance of Li–O_2 batteries was tested. We can see that the battery with LN can stably operate for 225 cycles at a current density of 500 mA g^{-1} and a cut-off capacity of 1000 mAh g^{-1} (Figure 4b), accompanied with a minimal increase of the discharge–charge overpotential before 200 cycles (Supporting Information, Figure S19). When increasing the cycling capacity to 2000 mAh g^{-1}, a long lifetime of 90 cycles can still be reached (Figure 4c). However, the battery with LiTFSI can only operate for 117 and 21 cycles at the limited capacities of 1000 and 2000 mAh g^{-1}, respectively (Figure 4e, f), much shorter than those of the batteries with LN.

To get insight into the influence of salt anions on cycling performance, in situ differential electrochemical mass spectrometry (DEMS) and ^{1}H nuclear magnetic resonance (^{1}H NMR) measurements were executed. Unlike the battery with LiTFSI that releases a great deal of CO_2 during the charge process (Figure 4h), there is negligible CO_2 evolution for the battery with LN (Figure 4g), signifying that the use of stable LN can promote the reversible decomposition of Li_2O_2 with fewer side reactions. This can be further validated by the less parasitic products (HCOOLi and CH_3COOLi) formed on the cathode of the LN-based battery after different cycles (Figure 4i, j; Supporting Information, Figure S20). Since the capture of LiO_2 by Nafion$^-$ can decrease the amount of free LiO_2, it is reasonable that the Li–O_2 battery with LN reduces the related parasitic reactions with LiO_2.[21] For the Li anode side, the one in LN possesses a more obvious metallic luster than that in LiTFSI (Supporting Information, Figure S21), revealing the efficacy of LN for protecting the Li anode in real Li–O_2 battery operation conditions. Thus, the superb cycling performance of the battery with LN is due to the synergetic contributions of Nafion$^-$-induced LiF-rich SEI for efficient Li protection and less parasitic reactions from the depressed activity of LiO_2. Given that the previous works demonstrated that high concentration electrolytes could induce the formation of high-quality SEI, we also compare the performance of the 0.5 M LN-based battery with that of the batteries with high concentration electrolytes. Different from the excellent rate capability of the LN-based battery, the performance of those

© 2022 Wiley-VCH GmbH

with high concentration electrolytes is rather poor (Supporting Information, Figure S22), which can be ascribed to the high viscosity induced sluggish mass transfer kinetics,[22] and the easily passivated cathodes by discharge products (Supporting Information, Figure S23), further proving the advantages of our designed LN-based polyelectrolyte solution.

Safety and Applications of Pouch Cell

As the safety of batteries is the premise for commercial applications, the flammability of the LN-based electrolyte was checked. We find that though the glass fiber membrane swollen with LN-based electrolyte can be ignited with a lighter, it shows low flammability and soon extinguishes (Figure 5a; Supporting Information, Video S1), while for that with LiTFSI-based electrolyte, it violently burns with the formation of black substances (Figure 5b; Supporting Information, Video S2). Then, a pouch-type Li–air cell that could power a red LED and electric fan was fabricated for further safety tests (Figure 5c, i; Supporting Information, Figure S24a, b, and Video S3). When the cell suffers from nail penetration (Figure 5d, e), its voltage is maintained pretty well without the occurrence of burning and short circuit (Supporting Information, Figure S24c). Moreover, the penetrated cell can still power the red LED and electric fan (Figure 5f, j; Supporting Information, Video S4), and its temperature just goes up several degrees (Figure 5g, h). Even when the cell further sustains a corner cutting, it can also power the electric fan and experiences a negligible voltage decay (Figure 5k; Supporting Information, Figure S24d and Video S5). All these tests reveal the superior safety of the Li–air battery with a LN-based electrolyte. Finally, the fabricated pouch cell was employed to power smart electronics. As expected, the cell can successfully charge a smartwatch with its power increasing from 57 % to 62 % in 7 minutes (Figure 5l, m), as well as supplying electricity for a smartphone (Figure 5n). The LN-based Li–

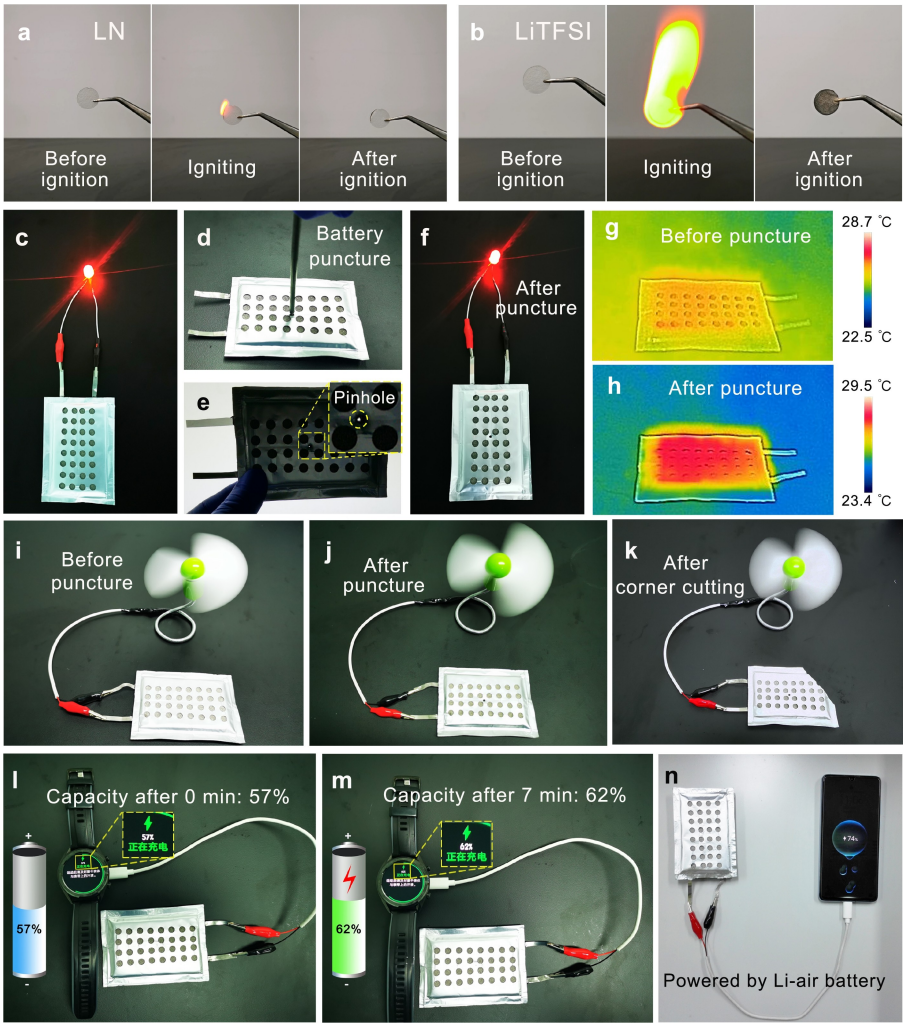

Figure 5. Flammability tests for the electrolytes of LN (a) and LiTFSI (b). Photographs of the red LED powered by the pouch cell before (c) and after puncture (f). Photographs of the puncture test (d, e) and the corresponding infrared thermal images (g, h). Photographs of the electric fan powered by the pouch cell before (i) and after puncture (j) and corner cutting (k). Photographs of the smartwatch (l, m) and smartphone (n) charged by the pouch cell.

© 2022 Wiley-VCH GmbH

air battery with satisfactory safety and an ability to provide power to veritable electronics exhibits promise towards practical applications.

Conclusion

In summary, a novel design strategy of polymerization and fluorination of the salt anions to satisfy the needs of high Li^+ transfer number and efficient Li protection for electrolyte has been proposed, and lithiated Nafion (LN) as a representative soluble perfluorinated polyanion has been introduced to prepare the polyelectrolyte solution, which delivers low flammability and a high Li^+ transfer number (0.84) and conductivity (2.5 mS cm^{-1}). The anions of the LN with a lower LUMO energy level than the solvent and strong interaction to LiO_2 can produce a LiF-rich SEI film for protecting the Li anode, and reduce the parasitic reactions associated with LiO_2. Benefiting from these advantages, we have successfully realized the application of the polyelectrolyte solution in Li–O_2 batteries. The LN-based polyelectrolyte solution endows the Li–O_2 battery with a low discharge–charge overpotential (0.30 V, energy efficiency 88.5 %), a large discharge capacity, an excellent rate capability, as well as a long lifetime. Furthermore, the pouch cells with LN-based electrolyte possess prominent safety and an ability to power commercial electronic equipment, exhibiting superb application prospects.

Acknowledgements

This work was financially supported by National Key R&D Program of China (2019YFA0705700), the National Natural Science Foundation of China (21725103), Key Research Program of the Chinese Academy of Sciences (ZDRW-CN-2021-3-3), and the K.C. Wong Education Foundation (GJTD-2018-09). The Supercomputing USTC is acknowledged for computational support.

Conflict of Interest

The authors declare no conflict of interest.

Data Availability Statement

The data that support the findings of this study are available from the corresponding author upon reasonable request.

Keywords: High Li^+ Transfer Number · Li–O_2 Battery · LiF-Rich Solid Electrolyte Interface · Lithiated Nafion · Polyelectrolyte Solution

[1] a) W. J. Kwak, Rosy, D. Sharon, C. Xia, H. Kim, L. R. Johnson, P. G. Bruce, L. F. Nazar, Y. K. Sun, A. A. Frimer, M. Noked, S. A. Freunberger, D. Aurbach, *Chem. Rev.* **2020**, *120*, 6626–6683; b) J. L. Ma, F. L. Meng, Y. Yu, D. P. Liu, J. M. Yan, Y. Zhang, X. B. Zhang, Q. Jiang, *Nat. Chem.* **2019**, *11*, 64–70; c) M. Asadi, B. Sayahpour, P. Abbasi, A. T. Ngo, K. Karis, J. R. Jokisaari, C. Liu, B. Narayanan, M. Gerard, P. Yasaei, X. Hu, A. Mukherjee, K. C. Lau, R. S. Assary, F. Khalili-Araghi, R. F. Klie, L. A. Curtiss, A. Salehi-Khojin, *Nature* **2018**, *555*, 502–506; d) Q. Xiong, G. Huang, X. B. Zhang, *Angew. Chem. Int. Ed.* **2020**, *59*, 19311–19319; *Angew. Chem.* **2020**, *132*, 19473–19481; e) Q. Lv, Z. Zhu, S. Zhao, L. Wang, Q. Zhao, F. Li, L. A. Archer, J. Chen, *J. Am. Chem. Soc.* **2021**, *143*, 1941–1947; f) G. Y. Qiao, D. Guan, S. Yuan, H. Rao, X. Chen, J. A. Wang, J. S. Qin, J. J. Xu, J. Yu, *J. Am. Chem. Soc.* **2021**, *143*, 14253–14260; g) X. Hu, G. Luo, Q. Zhao, D. Wu, T. Yang, J. Wen, R. Wang, C. Xu, N. Hu, *J. Am. Chem. Soc.* **2020**, *142*, 16776–16786; h) X. Chi, M. Li, J. Di, P. Bai, L. Song, X. Wang, F. Li, S. Liang, J. Xu, J. Yu, *Nature* **2021**, *592*, 551–557; i) J. Lai, Y. Xing, N. Chen, L. Li, F. Wu, R. Chen, *Angew. Chem. Int. Ed.* **2020**, *59*, 2974–2997; *Angew. Chem.* **2020**, *132*, 2994–3019; j) Z. Huang, H. Zeng, M. Xie, X. Lin, Z. Huang, Y. Shen, Y. Huang, *Angew. Chem. Int. Ed.* **2019**, *58*, 2345–2349; *Angew. Chem.* **2019**, *131*, 2367–2371.

[2] E. Strauss, S. Menkin, D. Golodnitsky, *J. Solid State Electrochem.* **2017**, *21*, 1879–1905.

[3] a) K. M. Diederichsen, E. J. McShane, B. D. McCloskey, *ACS Energy Lett.* **2017**, *2*, 2563–2575; b) Y. Liu, Y. Zhu, Y. Cui, *Nat. Energy* **2019**, *4*, 540–550.

[4] a) J. Wang, G. Huang, K. Chen, X. B. Zhang, *Angew. Chem. Int. Ed.* **2020**, *59*, 9382–9387; *Angew. Chem.* **2020**, *132*, 9468–9473; b) C. Zhao, Y. Zhu, Q. Sun, C. Wang, J. Luo, X. Lin, X. Yang, Y. Zhao, R. Li, S. Zhao, H. Huang, L. Zhang, S. Lu, M. Gu, X. Sun, *Angew. Chem. Int. Ed.* **2021**, *60*, 5821–5826; *Angew. Chem.* **2021**, *133*, 5885–5890.

[5] a) Q. Ma, H. Zhang, C. Zhou, L. Zheng, P. Cheng, J. Nie, W. Feng, Y. S. Hu, H. Li, X. Huang, L. Chen, M. Armand, Z. Zhou, *Angew. Chem. Int. Ed.* **2016**, *55*, 2521–2525; *Angew. Chem.* **2016**, *128*, 2567–2571; b) W. Zhang, S. Feng, M. Huang, B. Qiao, K. Shigenobu, L. Giordano, J. Lopez, R. Tatara, K. Ueno, K. Dokko, M. Watanabe, Y. Shao-Horn, J. A. Johnson, *Chem. Mater.* **2021**, *33*, 524–534; c) S. Li, A. I. Mohamed, V. Pande, H. Wang, J. Cuthbert, X. Pan, H. He, Z. Wang, V. Viswanathan, J. F. Whitacre, K. Matyjaszewski, *ACS Energy Lett.* **2018**, *3*, 20–27.

[6] E. R. Logan, J. R. Dahn, *Trends Chem.* **2020**, *2*, 354–366.

[7] a) K. M. Diederichsen, R. C. Terrell, B. D. McCloskey, *J. Phys. Chem. B* **2019**, *123*, 10858–10867; b) K. M. Diederichsen, K. D. Fong, R. C. Terrell, K. A. Persson, B. D. McCloskey, *Macromolecules* **2018**, *51*, 8761–8771.

[8] Z. Peng, S. A. Freunberger, Y. Chen, P. G. Bruce, *Science* **2012**, *337*, 563–566.

[9] a) K. Xu, *Chem. Rev.* **2014**, *114*, 11503–11618; b) X.-Q. Zhang, X.-B. Cheng, X. Chen, C. Yan, Q. Zhang, *Adv. Funct. Mater.* **2017**, *27*, 1605989.

[10] C. Cui, C. Yang, N. Eidson, J. Chen, F. Han, L. Chen, C. Luo, P. F. Wang, X. Fan, C. Wang, *Adv. Mater.* **2020**, *32*, 1906427.

[11] X. Fan, X. Ji, F. Han, J. Yue, J. Chen, L. Chen, T. Deng, J. Jiang, C. Wang, *Sci. Adv.* **2018**, *4*, eaau9245.

[12] a) S. Jurng, Z. L. Brown, J. Kim, B. L. Lucht, *Energy Environ. Sci.* **2018**, *11*, 2600–2608; b) M. Gauthier, T. J. Carney, A. Grimaud, L. Giordano, N. Pour, H. H. Chang, D. P. Fenning, S. F. Lux, O. Paschos, C. Bauer, F. Maglia, S. Lupart, P. Lamp, Y. Shao-Horn, *J. Phys. Chem. Lett.* **2015**, *6*, 4653–4672; c) L. Xing, X. Zheng, M. Schroeder, J. Alvarado, A. von Wald Cresce, K. Xu, Q. Li, W. Li, *Acc. Chem. Res.* **2018**, *51*, 282–289.

[13] a) Z. Zhang, L. Hu, H. Wu, W. Weng, M. Koh, P. C. Redfern, L. A. Curtiss, K. Amine, *Energy Environ. Sci.* **2013**, *6*, 1806–1810; b) W. Zhang, S. Zhang, L. Fan, L. Gao, X. Kong, S. Li, J.

© 2022 Wiley-VCH GmbH

Li, X. Hong, Y. Lu, *ACS Energy Lett.* **2019**, *4*, 644–650; c) Q. Zheng, Y. Yamada, R. Shang, S. Ko, Y.-Y. Lee, K. Kim, E. Nakamura, A. Yamada, *Nat. Energy* **2020**, *5*, 291–298.
[14] Gaussian 16A, G. W. T. M. J. Frisch, H. B. Schlegel, G. E. Scuseria, M. A. Robb, J. R. Cheeseman, G. Scalmani, V. Barone, et al., Gaussian, Inc., Wallingford CT, **2016**.
[15] a) D. Xu, Z. L. Wang, J. J. Xu, L. L. Zhang, X. B. Zhang, *Chem. Commun.* **2012**, *48*, 6948–6950; b) M. M. Ottakam Thotiyl, S. A. Freunberger, Z. Peng, P. G. Bruce, *J. Am. Chem. Soc.* **2013**, *135*, 494–500; c) Y. Chen, S. A. Freunberger, Z. Peng, O. Fontaine, P. G. Bruce, *Nat. Chem.* **2013**, *5*, 489–494.
[16] a) Y. Guo, P. Niu, Y. Liu, Y. Ouyang, D. Li, T. Zhai, H. Li, Y. Cui, *Adv. Mater.* **2019**, *31*, 1900342; b) Y. Yu, G. Huang, J.-Y. Du, J.-Z. Wang, Y. Wang, Z.-J. Wu, X.-B. Zhang, *Energy Environ. Sci.* **2020**, *13*, 3075–3081.
[17] a) J. Herranz, A. Garsuch, H. A. Gasteiger, *J. Phys. Chem. C* **2012**, *116*, 19084–19094; b) D. G. Kwabi, M. Tulodziecki, N. Pour, D. M. Itkis, C. V. Thompson, Y. Shao-Horn, *J. Phys. Chem. Lett.* **2016**, *7*, 1204–1212.
[18] T. Lu, F. Chen, *J. Comput. Chem.* **2012**, *33*, 580–592.
[19] I. Mayer, *Chem. Phys. Lett.* **1983**, *97*, 270–274.
[20] J. J. Xu, Z. W. Chang, Y. Wang, D. P. Liu, Y. Zhang, X. B. Zhang, *Adv. Mater.* **2016**, *28*, 9620–9628.
[21] a) Q. Zhao, N. Katyal, I. D. Seymour, G. Henkelman, T. Ma, *Angew. Chem. Int. Ed.* **2019**, *58*, 12553–12557; *Angew. Chem.* **2019**, *131*, 12683–12687; b) P. Zhang, L. Liu, X. He, X. Liu, H. Wang, J. He, Y. Zhao, *J. Am. Chem. Soc.* **2019**, *141*, 6263–6270.
[22] Y. Yamada, J. Wang, S. Ko, E. Watanabe, A. Yamada, *Nat. Energy* **2019**, *4*, 269–280.

Manuscript received: December 6, 2021
Version of record online: March 10, 2022

© 2022 Wiley-VCH GmbH